


 Cite this: *Lab Chip*, 2025, 25, 5055

Impact of sequential bifurcations on the cell-free layer of healthy and rigid red blood cells

 Yazdan Rashidi, *^a Christian Wagner ^{ab} and Steffen M. Recktenwald ^a

In the microcirculation, red blood cells (RBCs) tend to move away from vessel walls, creating a central flow of cells and a peripheral cell-free layer (CFL). The CFL significantly affects blood flow and is important for lab-on-a-chip applications, such as cell–plasma separation. This study investigates how the length of the feeding branch before bifurcations affects RBC distribution and CFL formation, especially in sequential T-bifurcations. We conducted experiments to study RBC flow in microfluidic bifurcating channels of different lengths (2.5–7.5 mm) at a fixed hematocrit of 5% using both healthy and artificially rigidified RBCs. Our findings show that a minimum branch length is required before a bifurcation to achieve a steady state in the CFL. If the channel length before a second bifurcation is shorter than this minimum, reaching an equilibrium CFL in sequential bifurcations is impossible. We observe that short channels after the first bifurcation lead to increased CFL asymmetry in the daughter branches after the second bifurcation, while longer channels better maintain symmetry. Additionally, we explored the impact of RBC rigidity on CFL development. Rigid and healthy RBCs showed similar behavior at the first bifurcation, but their CFL development patterns differed significantly by the second bifurcation, affecting RBC partitioning. These results emphasize the importance of considering branch length in the study and design of bifurcations for lab-on-a-chip devices and provide insights into how impaired RBC deformability can affect blood flow.

 Received 11th October 2024,
 Accepted 13th August 2025

DOI: 10.1039/d4lc00865k

rsc.li/loc

1 Introduction

The circulatory system is fundamental to the human body, facilitating the transport of oxygen and essential nutrients to organs through a complex network of blood vessels. This network, characterized by branching and bifurcating vessels, plays a significant role in influencing red blood cell (RBC) distribution and hematocrit partitioning.^{1,2} RBCs constitute approximately 45% of blood volume and are the primary cellular component of blood. In microcirculation, RBCs tend to migrate away from the vessel walls, leading to a central RBC flow and a peripheral cell-free layer (CFL). This spatial redistribution of RBCs has a profound impact on blood rheology by reducing the apparent viscosity in small vessels,^{3,4} and it critically influences the flow properties of blood *in vivo*.^{1,2} There, the presence of the CFL near vessel walls impacts various physiological processes, including platelet and leukocyte margination,^{5,6} the modulation of wall shear stress on endothelial cells,⁷ and the heterogeneous distribution of RBCs within branching vascular networks.^{8–11} In animal models, it has been shown that the mean width of

the CFL is directly related to vessel diameter, increasing from 0.8 μm in 10 μm arterioles to 2.9 μm in 50 μm arterioles.¹² The dynamics of RBCs traveling through sequentially diverging and converging bifurcations and the resulting RBC partition play a crucial role in the local cell perfusion in the microvascular system.

The spatial organization of RBCs and the formation of the CFL are also vital in biomedical lab-on-a-chip applications, particularly in microfluidic devices designed for cell and plasma separation and flow-focusing.^{13–17} Hence, the microscale collective behavior of RBCs, including their organization and the formation of a CFL near the vessel wall, has been the focus of extensive experimental^{10,18–22} and numerical investigations.^{8,23–26} It has been shown that the characteristics of the CFL in microchannels are influenced by several factors, such as the suspension hematocrit, channel dimensions, flow rate, and the biophysical properties of RBCs, particularly their deformability.^{17,22,27,28} The rigidity of RBCs is generally considered to impair blood flow and disrupt the spatiotemporal organization of RBCs in circulation. Decreased deformability in RBCs is a characteristic of various diseases, including malaria, diabetes, sickle cell disease, and acanthocytosis.^{29–33} Hence, measurement of RBC deformability, particularly in biomicrofluidic devices, has been the focus of numerous recent investigations.^{34–37}

^a *Dynamics of Fluids, Department of Experimental Physics, Saarland University, 66123 Saarbruecken, Germany. E-mail: yazdan.rashidi@uni-saarland.de*
^b *Physics and Materials Science Research Unit, University of Luxembourg, L-1511 Luxembourg, Luxembourg*


The arrangement and focusing of RBCs in dilute suspensions can be driven by geometric features of the channels, including confinement^{38–40} and bifurcations.^{41–43} In bifurcating channels, the higher flow rate daughter vessel often receives a higher RBC flow in relation to the volumetric flow rate, known as the Zweifach–Fung effect.⁴⁴ However, the opposite RBC partitioning can also occur when the higher flow rate channel receives a lower RBC flux in relation to the volumetric flow rate, depending on the vessel size and RBC flow configuration.⁴⁵ In microfluidic networks, Pskowski *et al.*⁴⁶ showed that hematocrit skewness along sequential bifurcations can induce significant changes in downstream RBC partitioning. The authors investigated the effect of the volumetric flow rates at each bifurcation, the solution hematocrit, and the channel length on the RBC flux and reported significant differences in partitioning between upstream and downstream bifurcations even when the flow rates in both channels are the same.⁴⁶ Similarly, it was observed that bifurcations downstream of the suspension inlet exhibited an inversion of RBC partitioning in idealized microfluidic networks, resulting in a heterogeneous RBC distribution.⁴⁷ While model microfluidic devices advance our understanding of blood flow in microvascular networks, the effect of geometrical parameters, such as the channel length before reaching the bifurcation, on the development and reformation of the CFL and its subsequent impact on the partitioning of RBCs in sequential bifurcations is not fully understood. Although our study did not directly measure rheological parameters such as apparent viscosity, it is well established that the CFL has a major influence on microvascular rheology.^{4,48,49} Symmetric CFL formation is likely to contribute to more uniform shear stress and flow resistance, while asymmetric CFLs may introduce local rheological heterogeneities.^{2,11,25} Additionally, the effect of biophysical cell properties, foremost impaired RBC deformability, on microcirculatory flow patterns has not been fully explored in the context of bifurcating networks.

This study investigates the evolution of RBC distribution along the flow direction in two sequential model bifurcations. Specifically, we examine how the flow rate and length affect CFL formation. We use model T-junctions, which produce a pronounced asymmetric CFL after the first bifurcation compared to other bifurcation shapes.⁴¹ Experiments are performed on healthy and artificially rigidified RBCs with a fixed hematocrit of 5% under various pressure drops and in microfluidic channels with different lengths for the first daughter channel, ranging from 2.5 mm to 7.5 mm. This study used a hematocrit of 5% to allow for detailed visualization and quantification of CFL dynamics in microchannels. While this is lower than physiological hematocrit levels, it enabled clearer observation of flow features. Although the flow rate has a significant influence on achieving steady-state flow and focusing on obtaining a symmetrical CFL at the end of each branch, our findings demonstrate that after the first bifurcation, a minimum

daughter channel length is required to achieve a symmetrical CFL before the second bifurcation. Additionally, we explore the impact of RBC rigidity on CFL formation. Although the differences between rigid and healthy RBCs were negligible at the first bifurcation, the development patterns of the CFL diverged significantly as they approached the second bifurcation. This divergence affects the partitioning of RBCs in the second bifurcation. Our work provides further insights into healthy and rigid RBC flow behavior at sequential bifurcations.

2 Materials and methods

2.1 Sample preparation

Blood was collected from healthy volunteers with informed consent using a finger prick. The collected blood was centrifuged at 1500g for 5 minutes to separate the components. The RBCs settled at the bottom were then resuspended in phosphate-buffered saline (PBS) solution (Gibco PBS, Fisher Scientific; Schwerte, Germany), and this centrifugation and washing process was repeated three times to ensure purity. After the final wash, the RBCs were diluted to achieve a hematocrit concentration of 5% in PBS containing 1 g L⁻¹ of bovine serum albumin (BSA, Sigma-Aldrich; Taufkirchen, Germany).⁵⁰

To assess the impact of rigidity, we artificially rigidified RBCs using a method previously described.⁴¹ Specifically, washed RBCs were incubated in a 0.1% glutaraldehyde (GA, Grade I solution, Merck KGaA, Darmstadt, Germany) solution for one hour, following the protocol established by Abay *et al.*⁵⁰ A 0.1% concentration of GA was chosen, as Abay *et al.*⁵⁰ showed that this concentration fixes RBCs and eliminates their deformability. After incubation, the RBCs were thoroughly washed with PBS to remove any residual GA and then suspended in a PBS/BSA solution at the same concentrations used for healthy RBCs. In this study, the term “rigid” refers to the GA-treated cells, in contrast to the naturally deformable healthy RBCs.

All procedures, including blood collection, sample preparation, and subsequent experiments, were conducted in accordance with the Declaration of Helsinki and the relevant national laws and guidelines of Germany, and were approved by the ethics committee of the “Aerzteammer des Saarlandes” at Saarland University (reference No. 24/12). Informed consent was obtained from all human participants prior to participation in the study.

2.2 Microfluidic setup

The microfluidic device used in this study was fabricated using standard soft lithography techniques with polydimethylsiloxane (PDMS, RTV 615A/B, Momentive Performance Materials, Waterford, NY).⁵¹ RBCs suspensions are pumped through the microfluidic chip featuring sequential T-junction geometries. The channel has a height of $H = 50 \mu\text{m}$ and consists of an inlet channel, known as the mother channel, with a width of $W_M = 100 \mu\text{m}$ and a length



of 2 cm in the flow direction. At the first T-bifurcation, the mother channel splits into two daughter outlet channels, each with a width of $W_{D1} = 50 \mu\text{m}$. In this study, the lengths of the first daughter channels are varied between $L_{D1} = 2.5 \text{ mm}$, 5 mm , and 7.5 mm , as depicted in Fig. 1. At the second T-bifurcation, each daughter channel splits into two outlet channels, each with a width of $W_{D2} = 50 \mu\text{m}$ and length of the $L_{D2} = 10 \text{ mm}$.

Rigid medical-grade polyethylene tubing with an inner diameter of 0.86 mm (Scientific Commodities, Lake Havasu City, AZ) connects the microfluidic device to both sample and waste containers. The device is mounted on an inverted microscope (Eclipse TE2000-S, Nikon, Melville, New York), equipped with LED illumination and a $20\times$ air objective (Plan Fluor, Nikon, Melville, NY) with a numerical aperture (NA) of 0.7 . A high-precision pressure control device (OB1-MK3, Elveflow, Paris, France) was employed to drive the RBC suspensions through the microchannels. The pressure device allowed for constant pressure drops to be applied across the channels, set at $p = 50 \text{ mbar}$, 100 mbar , 250 mbar , and 500 mbar .

2.3 Image processing and data analysis

To determine the thickness of the CFL, the flow of RBCs was recorded at different regions of interest (ROIs) along the flow direction. These ROIs, indicated by red boxes in Fig. 2(a), correspond to key positions in the microfluidic channel: the first bifurcation at the end of the mother branch, and the second bifurcation at the end of one of the first daughter channels. Due to the symmetry of the channel, we focused on one side of the channel, as depicted in Fig. 2(a).

It is challenging to distinguish individual cells at RBC concentrations above 1%, making it difficult to determine the CFL based on RBC trajectories alone. To address this, RBC flow was recorded using a high-speed camera (Fastec HiSpec 2G, FASTEC Imaging, San Diego, CA) at a frame rate of 100 frames per second. A custom MATLAB (9.14.0.2206163 (R2023a), The MathWorks, Natick, MA) algorithm was developed to analyze the recorded data and

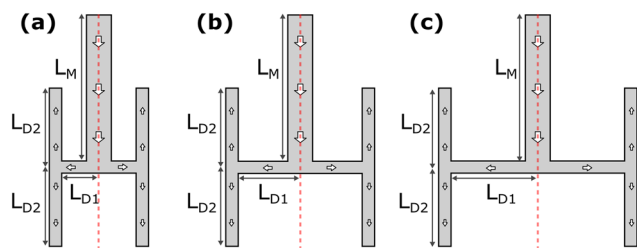


Fig. 1 Schematic representation of the used microfluidic channels. Each channel consists of two consecutive T-bifurcations in sequence with lengths of the first daughter branch of (a) $L_{D1} = 2.5 \text{ mm}$, (b) $L_{D1} = 5 \text{ mm}$, and (c) $L_{D1} = 7.5 \text{ mm}$. The lengths of the mother L_M and second daughter L_{D2} are kept constant for all three channels. Each channel is symmetric to the central axis, shown as red dashed lines.

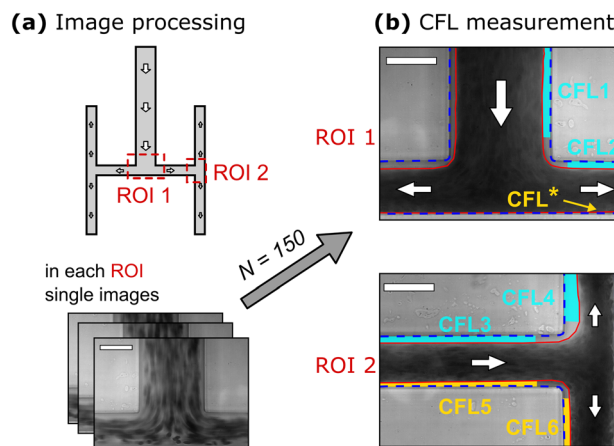


Fig. 2 Schematic representation of the experimental data analysis routine. Images are recorded in two regions of interest (ROI) along the flow direction, indicated by the red boxes in (a). In each ROI, 150 single images are stacked, and the RBC core flow and the channel walls are determined (see red and blue lines in (b)). Based on the positions of the RBCs and the walls, the CFL is determined along the flow direction (cyan and yellow areas). Data is shown for healthy RBCs at a pressure drop of 500 mbar for $L_{D1} = 2.5 \text{ mm}$. The scale bar represents $50 \mu\text{m}$.

calculate the CFL thickness. The CFL analysis process involved several steps. First, 150 images from the recorded image sequence were inverted and stacked. Then, the stacked images' pixel-wise standard deviation and median intensity were computed. Regions with high standard deviation correspond to areas with significant intensity fluctuations due to passing RBCs. We apply a threshold of 0.3% to detect regions of the core RBC flow, indicated by red lines in Fig. 2(b). In contrast, the median intensity was most noticeable at the stable channel borders throughout the image sequence. The median inverted intensity peak positions, corresponding to the channel borders, are also depicted in Fig. 2(b). Similar methods have been previously employed to detect the CFL at similar levels of hematocrit.⁴¹ The thickness of the CFL was calculated for each pixel line by the distance between the detected channel border and the detected RBC core flow. The CFL at various positions along the flow direction is illustrated with two different colors in Fig. 2(b): cyan represents the continuation of the CFL in the mother branch, while yellow represents the opposite side.

We further calculate the Reynolds number $Re = U_{\text{max}} D_h \rho / \eta$ in the rectangular microfluidic channel, where U_{max} is the maximum velocity in the channel center, D_h is the hydraulic diameter, ρ is the fluid density (1 g cm^{-3}), and η is the fluid's dynamic viscosity (1.2 mPa s). The hydraulic diameter is calculated as $D_h = 2WH / (W + H)$ for a channel with width W and height H . By employing particle image velocimetry (PIV) to measure the velocity profile across the channel, we determine the maximum velocity U_{max} . The calculated Reynolds number is between 2 and 20 for all channels and applied pressure drops, confirming that inertial forces play a role in RBC organization.



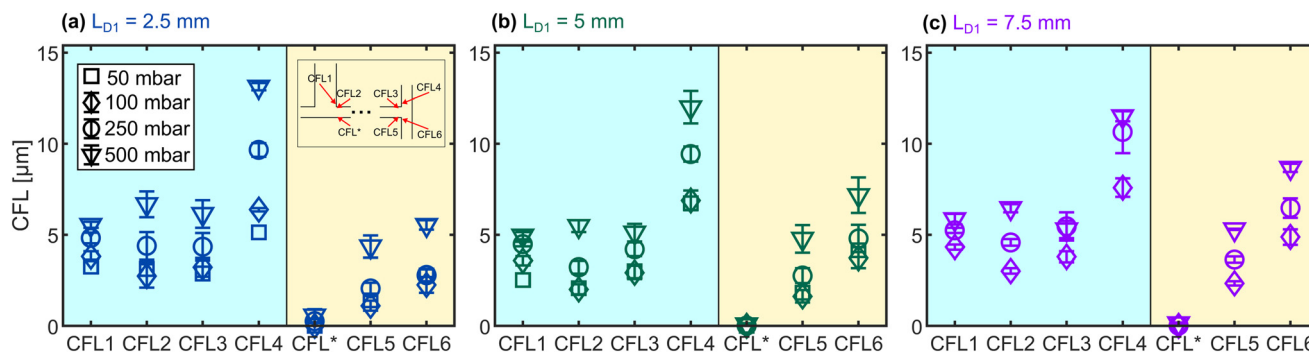


Fig. 3 The thickness of the CFL for different pressure drops (50, 100, 250, and 500 mbar) and different positions along the channel flow directions. In each panel, the background color indicates the CFL region, with cyan representing the top side and yellow representing the bottom side of the channel (see Fig. 2(b)). Panel (a–c) corresponds to the channel with the lengths of the first daughter branches being $L_{D1} = 2.5$ mm, $L_{D1} = 5$ mm, and $L_{D1} = 7.5$ mm, respectively, as shown in Fig. 1. The error bars represent the standard deviation of different measurements.

3 Results and discussion

3.1 CFL thickness along the flow direction

Fig. 3 summarizes the thickness of the CFL for healthy RBCs in the three used microfluidic devices for various positions along the flow direction, as explained in Fig. 2(b). Since the mother branches are the same in all three used channels, the CFL at the end of the mother (CFL1 in Fig. 3) is consistent for each channel. There is a slight increase in CFL1 as the pressure drop increases.

After the mother channel, we determined the thickness of the CFL in the first daughter channel at two positions, the inlet and the end of the branch, just before reaching the second bifurcation. At each position, we measured the CFL thickness on both the left (CFL2 and CFL3) and right sides (CFL* and CFL5) along the flow direction, as schematically shown by cyan and yellow colors in Fig. 2(b). CFL2 on the left side along the flow direction corresponds to the continuation of CFL1. However, we did not observe a pronounced CFL on the right side (CFL* ≈ 0) along the flow direction due to the flow splitting at the bifurcation and because RBCs are pushed against the wall at high flow rates. As the flow rate increases, which corresponds to an increase in Re, the CFL2 also increases, creating more asymmetry at the inlet of the daughter channel, meaning the difference in CFL thickness between the two sides of the branch (CFL2 and CFL*) becomes more pronounced. Since there are three different channels with varying lengths of the first daughter branch, the channel with the shortest daughter branch experiences a higher flow rate at the same applied pressure drop. This is illustrated in Fig. 3, where the channel with the shortest daughter branch shows more pronounced CFL asymmetry at the inlet of the daughter channel after the first bifurcation.

At the end of the first daughter channel, CFL3 represents the left side, and CFL5 represents the right side along the flow direction. After the first bifurcation (inlet of the daughter channel), we observed asymmetry in the CFL for all the channels. However, in the channel where the first daughter branch is longer ($L_{D1} = 7.5$ mm), as shown in Fig. 3(c), CFL3 and CFL5, are more closely aligned at a

pressure of 500 mbar (Re = 15). This indicates that the length of this daughter channel was sufficient to restore symmetry in the CFL and reach a steady state. In contrast, in the channel with the shorter daughter branch ($L_{D1} = 2.5$ mm), as shown in Fig. 3(a), the CFL remains asymmetric despite the same maximum pressure of 500 mbar (Re = 20), which can impact the flow partitioning at the second bifurcation.

After the second bifurcation, we determined the CFL thickness in the subsequent daughter branches, focusing on the sides that continue from the CFL at the end of the first daughter branches. The CFL thickness is labeled as CFL4 for the top daughter branch, while for the bottom daughter branch, it is labeled as CFL6. The results show that for the channel with a first daughter branch length ($L_{D1} = 2.5$ mm), the CFL values in the daughter branches are different, with one branch having a thicker CFL than the other. This difference becomes more pronounced as the pressure increases. This is because the shorter length of the first daughter branch was not sufficient to restore symmetry in the CFL before reaching the second bifurcation. In contrast, for the channel with a longer first daughter branch ($L_{D1} = 7.5$ mm), the CFL values in the daughter branches after the second bifurcation are much closer to each other. This

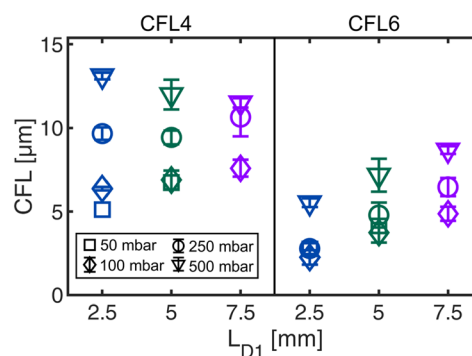


Fig. 4 The thickness of the CFL4 and CFL6 in the last daughter branches after the second bifurcation for various pressure drops as a function of the length of the previous daughter L_{D1} . The error bars represent the standard deviation of different measurements.



symmetry in the CFL thickness for the daughter branches after the second bifurcation is due to the length of the first daughter branch, which provided sufficient distance for the CFL to stabilize and become symmetric before reaching the second bifurcation even at higher flow velocities.

Fig. 4 emphasizes the results for CFL4 and CFL6 on how geometry and flow rate influence the development of asymmetric CFL in symmetric bifurcations. For CFL4, the thickness of the CFL decreases with increasing channel length at 500 mbar, while it seems to increase at lower pressure drops. Hence, increasing the length of the first daughter branches appears to reduce the influence of the flow rate on CFL4, suggesting that the flow has less impact on creating asymmetry in this case. In contrast, for CFL6, the CFL thickness consistently increases with the length of the daughter branches. The results indicate that the most significant asymmetry for the daughter channel after the second bifurcation occurs when the first daughter branch is short and the flow rate is high. Interestingly, our findings suggest that a minimum length for the first daughter branch is necessary to avoid significant asymmetry in the daughter branches after the second bifurcation.

The CFL phenomenon results from the interplay of hydrodynamic forces, which have been extensively studied.^{1–3,41,52,53} These forces cause the migration of cells and particles to specific positions within the flow, leading to the formation of the CFL. Lateral migration and particle focusing in circular pipes due to inertial lift forces were initially observed by Segré and Silberberg.⁵⁴ This phenomenon of inertial focusing is primarily influenced by two opposing forces. The first is the wall-induced lift force, which arises from the interaction between the particle and the channel wall, causing the particle to move away from the wall. The second is the shear gradient-induced lift force, which results from the velocity profile's curvature within the channel, pushing the particle away from the channel's center.^{52,53} These forces collectively guide particles and cells toward specific equilibrium positions within the channel cross-section. These positions are determined by factors such as the channel geometry, particle size and rigidity, and flow velocity. In square or rectangular microchannels, particle focusing is typically achieved when the particle Re number is on the order of one or greater. Additionally, a certain length L_f is necessary for particles to stabilize at their equilibrium positions along the flow direction.⁵² The formation of a CFL in RBC suspensions flowing through microfluidic channels, as described by Secomb *et al.*,² is a phenomenon primarily driven by the lateral migration of RBCs toward the center of the channel. This migration leads to the development of a plasma-rich layer devoid of cells near the channel walls. Due to its significant impact on flow resistance and the transport of platelets and particles in microcirculatory blood flow, the CFL has been extensively investigated through *in vivo*, *in vitro*, and *in silico* studies.^{17,23,27} However, most of this research has focused on the behavior of the CFL under varying blood flow conditions in a straight vessel or channel.

Recent studies have shown that the asymmetry in cell focusing that occurs after a bifurcation can significantly modify the distribution of RBCs in subsequent bifurcations.^{11,43,55,56} Furthermore, it has been demonstrated that at low hematocrit levels, RBC flow tends to deviate from the Zweifach–Fung effect, with cell deformability playing a crucial role in this reversed partitioning behavior.⁴³

Previous studies have demonstrated that the thickness of the CFL, once it reaches a steady state, can be independent of channel diameter,^{10,23,57} particularly when the diameter exceeds 10 μm . Our findings confirm this by looking at the steady-state CFL at the ends of the mother branches and the first daughter channel in the case with the longest daughter length and highest pressure drop. In this case, the CFL thickness was approximately 6 μm , despite the mother channel having a diameter of 100 μm and the daughter channel a diameter of 50 μm . Notably, the CFL thickness remained comparable in both channels. These results are consistent with those reported by Maeda *et al.*,⁵⁸ who observed a CFL thickness of 6 μm in channels with a diameter of 35 μm and a hematocrit of 8%.

3.2 CFL before the bifurcations

Starting with a random distribution of RBCs at the inlet, a certain minimum length of the channel is required for the CFL to fully develop. As RBCs migrate toward the center, the CFL gradually forms along the length of the channel. The CFL formation was investigated along the mother branch, with measurements taken at the end of this branch just before the first bifurcation (CFL1) with the length of 20 mm. Fig. 5(a) shows how the CFL1 changes as a function of velocity. Since the mother branch is same for all channels, the primary parameter that determines the CFL1 is the velocity profile. The results demonstrate that when the maximum velocity of the velocity profile in the channel exceeds approximately 200 mm s^{-1} , the CFL seems to reach a steady-state thickness of approximately 5 μm , in agreement with previous studies.¹⁰ This suggests that for effective CFL formation, the flow rate must be controlled, and the channel length must be sufficient to allow RBCs enough time to migrate and establish the CFL.

Fig. 5(b and c) shows the CFL thickness at the end of the first daughter branch for the left (CFL3) and right (CFL5) sides along the flow direction, respectively, as a function of the RBCs velocity. After the first bifurcation, the CFL “resets”, meaning that the symmetry in CFL thickness on both sides of the channel is no longer maintained. As a result, we observe asymmetry in the CFL at the inlet of the first daughter branches. We examined how this CFL develops along the first daughter channel, particularly at the end of the channel before the second bifurcation. For CFL3, we found that the CFL seems to reach a steady state again, when the velocity is larger than approximately 200 mm s^{-1} , similar to the mother channel. Despite the diameter of the mother channel being larger than that of the daughter channel, the



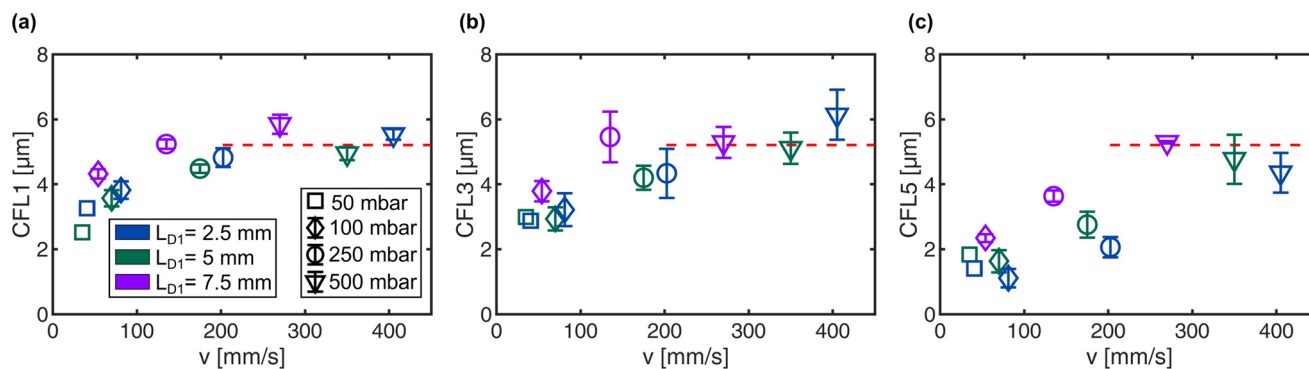


Fig. 5 Development of the CFL before the bifurcations (CFL1, CFL3, and CFL5) as a function of the velocity. The first panel (a) shows the region CFL1 at the end of the first mother branch. Panels (b) and (c) correspond to the ends of the first daughter branches before the second bifurcation, labeled as CFL3 and CFL4, respectively. The dashed red line represents the average value of CFL1 when the velocity exceeds 200 mm s^{-1} and reaches a steady state. The dashed red line represents the thickness of the CFL when it reaches a steady state. The error bars represent the standard deviation of different measurements.

steady-state thickness of the CFL remains the same. This indicates that, for high concentrations of blood (in our case 5%), the width of the channel only has a minor effect on the steady-state thickness of the CFL compared to the flow velocity. In contrast, the right side along the flow direction of the channel shows a different trend (Fig. 5(c)). Here, the CFL thickness exhibits an increase with increasing velocity without saturating, suggesting that a steady state has not yet been reached for CFL5.

Previous work has already explored the growth of the CFL along the flow direction in straight microfluidic channels. Amini *et al.*⁵² studied straight channels with a hydraulic diameter of $48 \mu\text{m}$ and particles with a diameter of $10 \mu\text{m}$, finding that the minimum length required for particle focusing is approximately 2 cm, given a particle Reynolds number of 3.3. The particle Reynolds number is defined as $Re_p = Re(a/D_h)^2$, where a is the particle diameter and D_h is the hydraulic diameter of the channel. Our microfluidic chip designs also feature mother branches that are 2 cm in length. As shown in Fig. 5(a), the thickness of the CFL becomes stable at the end of this branch when the flow velocity exceeds 200 mm s^{-1} ($Re = 10$ and $Re_p = 0.14$), which is lower than previously reported for rigid beads.⁵²

Moreover, Zhou *et al.*¹¹ recently explored CFL growth in a straight rectangular channel with dimensions comparable to the mother channel used in our study. They conducted numerical simulations and microfluidic experiments at negligible inertia ($Re < 1$). At low RBC concentrations, they observed that the CFL grew according to a power-law behavior, with exponents ranging from 0.26 to 0.4. In their simulations, the CFL increased over a length of $28L/D_h$ without reaching saturation, while in their microfluidic experiments, CFL growth extended over more than $46D_h$ without reaching equilibrium at RBC concentrations of 1%. In our study, conducted at $Re > 1$, we examined three different microfluidic chips with daughter branch lengths of approximately $37D_h$, $75D_h$, and $115D_h$. Similar to the results of Zhou *et al.*,¹¹ our results indicate that these lengths are

insufficient for the RBCs to achieve a steady state and symmetric CFL thickness on both sides of the daughter branches before reaching the second bifurcation (Fig. 5(c)). However, in the channel with the longest daughter branches and at higher flow rates, there is a noticeable trend toward achieving symmetry in CFL thickness on both sides, as shown in Fig. 3(c).

Our results also reveal that, although CFL3 reaches a steady state at velocities greater than 200 mm s^{-1} (Fig. 5(b)), CFL5 continues to exhibit an increase in CFL thickness as velocity increases, indicating that it has not yet reached a steady state, as shown in Fig. 5(c). This lack of symmetry in CFL thickness can significantly impact the daughter branches after the second bifurcation, as the evolution of the lower CFL remains uneven. Although increasing Re can reduce the minimum length required to reach a steady state, our results show that after the first bifurcation, a certain minimum length is still needed to achieve steady-state conditions due to the non-uniform distribution of RBCs.

3.3 Effect of cell rigidity on the CFL

As described in the image processing and data analysis section, pixel-wise standard deviation and median intensity were computed from the image stack. Regions with high standard deviation indicate areas with significant intensity fluctuations caused by the passage of RBCs. These fluctuations allowed us to calculate the core flow of RBCs at various positions along the channel. Here, we present a comparison between rigid and healthy RBCs based on the RBC core flow distribution at five different positions in the channel: two positions at the first bifurcation and three positions at the second bifurcation (P1–P5 in Fig. 6(a)). Due to the symmetry in the first bifurcation, only one daughter channel was analyzed, as the other branch exhibits the same behavior. However, in the second bifurcation, despite the geometric symmetry, the asymmetry in the CFL formed after the first bifurcation



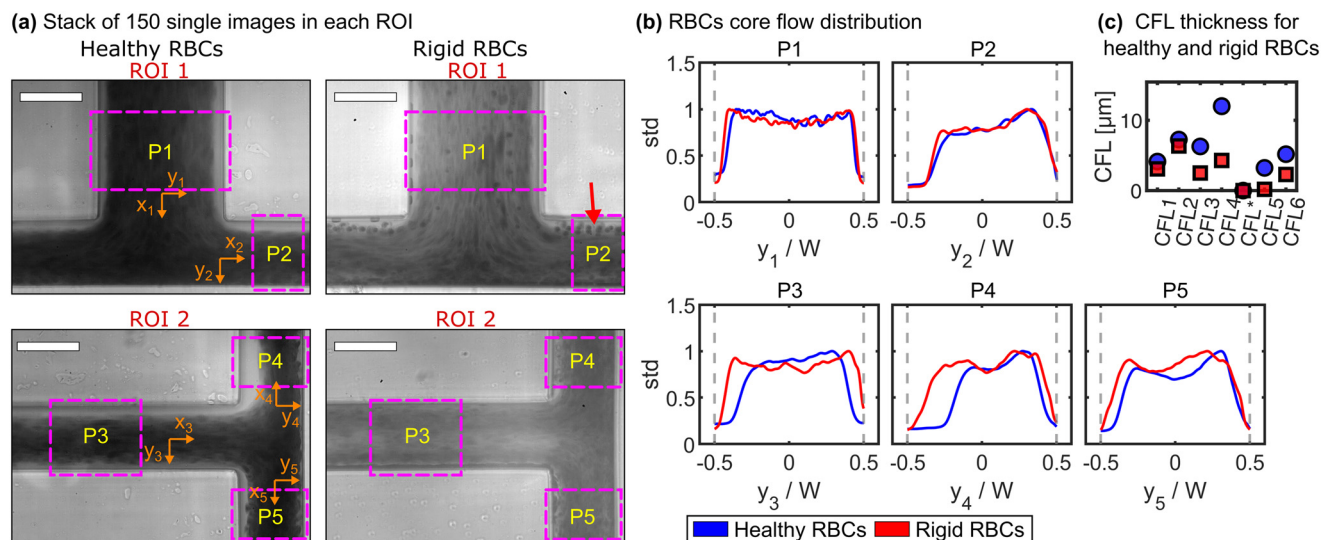


Fig. 6 Comparison between healthy and rigid RBC flow at five distinct positions within the channel, as indicated in panel (a). In each ROI, 150 single images were stacked. The first two positions correspond to the first bifurcation, while the remaining three are located at the second bifurcation, labeled P1 to P5 in the figure. The scale bar represents 50 μm . (b) Stacked images' pixel-wise standard deviation and median intensity were computed to identify the core RBC flow's channel border and boundary. Regions with high standard deviation indicate areas with significant intensity fluctuations corresponding to the core RBC flow. These areas are represented in blue for healthy cells and red for rigid cells. The gray dashed lines mark the channel walls. (c) The CFL thickness for both rigid and healthy cells, determined using a 0.3% threshold based on the pixel-wise standard deviation of stacked images, is shown in panel b.

can lead to differences in the daughter branches after the second bifurcation. Therefore, both daughter branches were analyzed after the second bifurcation. In addition to the dependency of the CFL on flow rate and daughter channel length, we discovered that at all analyzed positions, the core flow of the RBCs for rigid cells is wider than for healthy RBCs. Although the differences at positions P1 and P2 are not significant, the results in Fig. 6 show that the differences become more pronounced at positions P3, P4, and P5. Since the core flow of rigid RBCs is wider than that of healthy RBCs, the CFL for rigid RBCs is consistently smaller than for healthy RBCs, in agreement with previous studies.^{9,10,40,41,59} To address this, we applied the same threshold used for healthy RBCs to evaluate the CFL thickness for rigid RBCs. The results, presented in Fig. 6(c), indicate that the CFL thickness is consistently smaller for rigid RBCs compared to healthy RBCs across all regions.

Both populations have a uniform distribution at the inlet of the mother branch, as demonstrated in previous studies.⁴¹ At position P1, which is located at the end of the mother branch, there is no obvious difference between the rigid and healthy RBCs, and the core flow for both cell types is quite similar overall, as shown in Fig. 6. After the first bifurcation, at the inlet of the first daughter channel (position P2), the differences become more pronounced in the stacked images. In the CFL region, some rigid cells are seen flowing closer to the wall, which is shown by the red arrow in Fig. 6(a). This asymmetry in the CFL after the first bifurcation helps us understand the effect of the initial distribution and differing behavior between rigid and healthy RBCs in the flow, which

becomes evident at the end of this branch and just before the second bifurcation.

At position P3, as shown in Fig. 6, just before the second bifurcation, there is a significant difference between rigid and healthy cells. For healthy cells, the CFL develops symmetrically on both sides of the channel, while for rigid cells, more cells are observed sliding along the wall. The core flow for rigid cells at P3 occupies almost the entire channel width, whereas, for healthy cells, the core flow is more concentrated toward the center. The difference between rigid and healthy cells before the second bifurcation can be attributed to two factors. First, the initial distribution after the first bifurcation of RBCs is non-uniform and skewed toward one side of the channel, in agreement with previous studies on single T-junctions.⁴¹ Due to differences in deformability, the lateral migration behavior of healthy and rigid RBCs varies significantly. Healthy RBCs, being more deformable, tend to migrate more effectively toward the center of the channel, while rigid RBCs exhibit less lateral migration, remaining closer to the channel walls. Second, the sliding of rigid RBCs into the CFL area at position P2, highlighted by the red arrow in Fig. 6(a). These differences between rigid and healthy RBCs can significantly affect partitioning and CFL formation in the subsequent daughter branches, as observed at positions P4 and P5.

Shen *et al.*⁴³ demonstrated that altering cell deformability can lead to deviations from the Zweifach–Fung effect, resulting in inverse partitioning of RBCs at bifurcations. As shown in Fig. 6, we found that the development of the CFL after the first bifurcation, before reaching the second bifurcation, can be significantly influenced by cell



deformability. The differences in core flow between rigid and healthy cells before the second bifurcation can lead to pronounced discrepancies and asymmetry in the daughter branches downstream. Masaeli *et al.*⁶⁰ demonstrated that the inertial separation of particles with different shapes is both possible and tunable by adjusting channel geometry and flow conditions. They showed that spherical particles tend to focus closer to the channel wall, while more ellipsoid particles focus towards the center of the channel. Our results align with their findings, as we observed that rigid particles, which cannot deform and are more spherical in shape, result in a thinner CFL, while healthy cells result in a thicker CFL. Additionally, their results showed that spherical particles' lateral migration is less pronounced than ellipsoid particles. We observed a similar trend in the development of the CFL after the first bifurcation, where the lateral migration is more significant for healthy cells compared to rigid RBCs. This is evident in Fig. 6(b) at position P3, which shows the core flow of the particles before reaching the second bifurcation. It demonstrates that healthy RBCs tend to reach a steady state before the second bifurcation more easily than rigid cells. As shown in P3 in Fig. 6, the CFL develops on both sides of the channel for healthy cells, which is not the case for rigid RBCs.

4 Conclusions

Studying the effect of lateral migration, which is directly correlated with the thickness of the CFL in microfluidic flows, enhances our understanding of blood flow *in vivo*. It is essential to understand how changes in the CFL influence hemorheology, particularly in complex geometries such as bifurcating vessels and networks. In this study, we performed microfluidic measurements at various positions along the channel flow direction in three different microfluidic chips, each with varying lengths of the first daughter branches before reaching the second bifurcation, with a fixed hematocrit of 5%. We designed the daughter branches with lengths of 2.5 mm, 5 mm, and 7.5 mm to investigate the impact of CFL development on RBC flow behavior and to determine the minimum length required for RBCs to achieve a steady state. Additionally, we examined the effect of RBC rigidity on CFL development, which is crucial for understanding the impact of pathological changes in RBCs on their flow properties and the development of the CFL. Our study focused on a binary comparison between healthy and rigidified RBCs, future investigations could explore a continuum of rigidity using diamide, which allows for controlled, gradual stiffening of RBCs.²⁸ Such experiments would help validate the sensitivity of our method to subtle biomechanical changes and may support its utility in pathological contexts where RBC deformability is progressively altered.

At the first bifurcation, we observed that increasing the flow rate led to increasing asymmetry in the daughter branches after the bifurcation. In our experiments, conducted

at a hematocrit of 5%, we noticed that a significant portion of the rigid RBCs tended to slide along the walls without moving away from them – a behavior not observed with healthy RBCs. Upon reaching the second bifurcation, we found that a minimum branch length is required to achieve steady-state CFL thickness before the bifurcation. For microfluidic chips with shorter daughter branches, increasing the flow rate increased the asymmetry at the inlet of the first-daughter branches, making it impossible to reach steady-state CFL thickness before the second bifurcation. However, in microfluidic chip with longer daughter branches, increasing the flow rate allowed the CFL to reach a steady state before the second bifurcation. This study maintained consistent channel widths in the second bifurcation, variations in downstream channel width are expected to affect the absolute thickness of the CFL. Narrower channels would likely reduce CFL thickness, whereas wider channels would permit greater lateral migration of RBCs. While we use a hematocrit of 5% to visualize the CFL in this study, Future studies may extend this analysis to higher hematocrit regimes (*e.g.*, 20–45%) using improved imaging techniques to investigate the robustness of observed phenomena under more physiologically relevant conditions. Our *in vitro* microfluidic experiments on CFL development demonstrate that achieving a steady state of the CFL thickness before a bifurcation strongly depends on the length of the mother branch leading into the bifurcation. These findings emphasize the importance of considering the mother branch length in designing complex vascular networks, as it is crucial for maintaining uniform CFL development and flow behavior, and should also be taken into account when studying *in vivo* complex networks.

Author contributions

Y. R. and S. M. R. designed research; Y. R. performed experiments; S. M. R. and Y. R. analyzed data; Y. R., S. M. R., and C. W. wrote the paper.

Conflicts of interest

There are no conflicts of interest to declare.

Data availability

The data supporting this study's findings are available through the OneDrive link provided in the Zenodo dataset, accessible *via* <https://doi.org/10.5281/zenodo.13913455>.

Acknowledgements

This research was funded by the Deutsche Forschungsgemeinschaft (DFG, German Research Foundation) – project number 349558021 (WA 1336/13-1 and RE 5025/1-2). We would like to express our gratitude to Dr. Alexis Darras for the valuable scientific discussions and insights that contributed to the development of this paper.



The authors are also grateful to MicroFabSpace and Microscopy Characterization Facility, Unit 7 of ICTS 'NANBIOSIS' from CIBER-BBN at IBEC for preparing the microfluidic chips.

Notes and references

- 1 A. R. Pries and T. W. Secomb, *Microcirculation*, Elsevier, 2008, pp. 3–36.
- 2 T. W. Secomb, *Annu. Rev. Fluid Mech.*, 2017, **49**, 443–461.
- 3 R. Fåhræus, *Physiol. Rev.*, 1929, **9**, 241–274.
- 4 R. Fåhræus and T. Lindqvist, *American Journal of Physiology-Legacy Content*, 1931, **96**, 562–568.
- 5 J. B. Freund, *Phys. Fluids*, 2007, **19**, 023301.
- 6 H. Zhao, E. S. Shaqfeh and V. Narsimhan, *Phys. Fluids*, 2012, **24**, 011902.
- 7 P. F. Davies and S. C. Tripathi, *Circ. Res.*, 1993, **72**, 239–245.
- 8 P. Balogh and P. Bagchi, *J. Fluid Mech.*, 2019, **864**, 768–806.
- 9 D. Bento, A. I. Pereira, J. Lima, J. M. Miranda and R. Lima, *Comput. Methods Biomech. Biomed. Eng. Imaging Vis.*, 2018, **6**, 629–637.
- 10 D. Bento, C. S. Fernandes, J. M. Miranda and R. Lima, *Exp. Therm. Fluid Sci.*, 2019, **109**, 109847.
- 11 Q. Zhou, J. Fidalgo, M. O. Bernabeu, M. S. Oliveira and T. Krüger, *Soft Matter*, 2021, **17**, 3619–3633.
- 12 S. Kim, R. L. Kong, A. S. Popel, M. Intaglietta and P. C. Johnson, *Am. J. Physiol.*, 2007, **293**, H1526–H1535.
- 13 S. Yang, A. Ündar and J. D. Zahn, *Lab Chip*, 2006, **6**, 871–880.
- 14 E. Sollier, M. Cubizolles, Y. Fouillet and J.-L. Achard, *Biomed. Microdevices*, 2010, **12**, 485–497.
- 15 M. G. Lee, S. Choi, H.-J. Kim, H. K. Lim, J.-H. Kim, N. Huh and J.-K. Park, *Appl. Phys. Lett.*, 2011, **98**, 253702.
- 16 D. Pinho, T. Yaginuma and R. Lima, *BioChip J.*, 2013, **7**, 367–374.
- 17 S. Tripathi, Y. B. V. Kumar, A. Prabhakar, S. S. Joshi and A. Agrawal, *J. Micromech. Microeng.*, 2015, **25**, 083001.
- 18 G. Bugliarello and J. Sevilla, *Biorheology*, 1970, **7**, 85–107.
- 19 B. M. Fenton, R. T. Carr and G. R. Cokelet, *Microvasc. Res.*, 1985, **29**, 103–126.
- 20 R. Lima, T. Ishikawa, Y. Imai, M. Takeda, S. Wada and T. Yamaguchi, *J. Biomech.*, 2008, **41**, 2188–2196.
- 21 Q. Zhou, J. Fidalgo, L. Calvi, M. O. Bernabeu, P. R. Hoskins, M. S. Oliveira and T. Krüger, *Biophys. J.*, 2020, **118**, 2561–2573.
- 22 S. M. Recktenwald, K. Graessel, Y. Rashidi, J. N. Steuer, T. John, S. Gekle and C. Wagner, *Phys. Rev. Fluids*, 2023, **8**, 074202.
- 23 D. A. Fedosov, B. Caswell, A. S. Popel and G. E. Karniadakis, *Microcirculation*, 2010, **17**, 615–628.
- 24 X. Yin and J. Zhang, *Biorheology*, 2012, **49**, 261–270.
- 25 D. Katanov, G. Gompper and D. A. Fedosov, *Microvasc. Res.*, 2015, **99**, 57–66.
- 26 K. Vahidkhan, P. Balogh and P. Bagchi, *Sci. Rep.*, 2016, **6**, 28194.
- 27 S. Kim, P. K. Ong, O. Yalcin, M. Intaglietta and P. C. Johnson, *Biorheology*, 2009, **46**, 181–189.
- 28 M. Nouaman, A. Darras, C. Wagner and S. M. Recktenwald, *Biomicrofluidics*, 2024, **18**, 024104.
- 29 J. Stuart and G. Nash, *Blood Rev.*, 1990, **4**, 141–147.
- 30 A. Dondorp, M. Nyanoti, P. Kager, S. Mithwani, J. Vreeken and K. Marsh, *Trans. R. Soc. Trop. Med. Hyg.*, 2002, **96**, 282–286.
- 31 A. Symeonidis, G. Athanassiou, A. Psiroyannis, V. Kyriazopoulou, K. Kapatais-Zoumbos, Y. Missirlis and N. Zoumbos, *Clin. Lab. Haematol.*, 2001, **23**, 103–109.
- 32 R. Mannino, D. R. Myers, Y. Sakurai, R. E. Ware, G. Barabino and W. Lam, *Blood*, 2012, **120**, 818.
- 33 F. Reichel, M. Kräter, K. Peikert, H. Glaß, P. Rosendahl, M. Herbig, A. Rivera Prieto, A. Kihm, G. Bosman and L. Kaestner, *et al.*, *Front. Physiol.*, 2022, **13**, 852946.
- 34 G. Tomaiuolo, *Biomicrofluidics*, 2014, **8**, 051501.
- 35 Y. Man, E. Kucukal, R. An, Q. D. Watson, J. Bosch, P. A. Zimmerman, J. A. Little and U. A. Gurkan, *Lab Chip*, 2020, **20**, 2086–2099.
- 36 K. Matthews, E. S. Lamoureux, M.-E. Myrand-Lapierre, S. P. Duffy and H. Ma, *Lab Chip*, 2022, **22**, 1254–1274.
- 37 E. S. Lamoureux, E. Islamzada, M. V. J. Wiens, K. Matthews, S. P. Duffy and H. Ma, *Lab Chip*, 2022, **22**, 26–39.
- 38 G. Tomaiuolo, L. Lanotte, G. Ghigliotti, C. Misbah and S. Guido, *Phys. Fluids*, 2012, **24**, 051903.
- 39 C. Iss, D. Midou, A. Moreau, D. Held, A. Charrier, S. Mendez, A. Viallat and E. Helfer, *Soft Matter*, 2019, **15**, 2971–2980.
- 40 A. Abay, S. M. Recktenwald, T. John, L. Kaestner and C. Wagner, *Soft Matter*, 2020, **16**, 534–543.
- 41 Y. Rashidi, O. Aouane, A. Darras, T. John, J. Harting, C. Wagner and S. M. Recktenwald, *Soft Matter*, 2023, **19**, 6255–6266.
- 42 J. M. Sherwood, D. Holmes, E. Kaliviotis and S. Balabani, *PLoS One*, 2014, **9**, e100473.
- 43 Z. Shen, G. Coupier, B. Kaoui, B. Polack, J. Harting, C. Misbah and T. Podgorski, *Microvasc. Res.*, 2016, **105**, 40–46.
- 44 K. Svanes and B. Zweifach, *Microvasc. Res.*, 1968, **1**, 210–220.
- 45 P. Balogh and P. Bagchi, *Phys. Fluids*, 2018, **30**, 051902.
- 46 A. Pskowski, P. Bagchi and J. D. Zahn, *Biomicrofluidics*, 2022, **16**, 064104.
- 47 A. Mantegazza, F. Clavica and D. Obrist, *Biomicrofluidics*, 2020, **14**, 014101.
- 48 F. Cuomo, J. Ferruzzi, J. D. Humphrey and C. A. Figueroa, *Ann. Biomed. Eng.*, 2015, **43**, 1555–1570.
- 49 A. R. Pries, D. Neuhaus and P. Gaetgens, *Am. J. Physiol.*, 1992, **263**, H1770–H1778.
- 50 A. Abay, G. Simionato, R. Chachanidze, A. Bogdanova, L. Hertz, P. Bianchi, E. van den Akker and M. von Lindern, *Front. Physiol.*, 2019, **10**, 1–14.
- 51 J. Friend and L. Yeo, *Biomicrofluidics*, 2010, **4**, 026502.
- 52 H. Amini, W. Lee and D. Di Carlo, *Lab Chip*, 2014, **14**, 2739–2761.
- 53 D. Di Carlo, *Lab Chip*, 2009, **9**, 3038–3046.
- 54 G. Segré and A. Silberberg, *Nature*, 1961, **189**, 209–210.
- 55 A. Mantegazza, F. Clavica and D. Obrist, *Biomicrofluidics*, 2020, **14**, 014101.



- 56 A. Merlo, M. Berg, P. Duru, F. Risso, Y. Davit and S. Lorthois, *Soft Matter*, 2022, **18**, 1463–1478.
- 57 S. Yamaguchi, T. Yamakawa and H. Niimi, *Biorheology*, 1992, **29**, 251–260.
- 58 N. Maeda, Y. Suzuki, J. Tanaka and N. Tateishi, *Am. J. Physiol.*, 1996, **271**, H2454–H2461.
- 59 H. Fujiwara, T. Ishikawa, R. Lima, N. Matsuki, Y. Imai, H. Kaji, M. Nishizawa and T. Yamaguchi, *J. Biomech.*, 2009, **42**, 838–843.
- 60 M. Masaeli, E. Sollier, H. Amini, W. Mao, K. Camacho, N. Doshi, S. Mitragotri, A. Alexeev and D. Di Carlo, *Phys. Rev. X*, 2012, **2**, 031017.

